Spindle-shaped CeO₂/biochar carbon with oxygen-vacancy as an effective and highly durable electrocatalyst for oxygen reduction reaction

Narayanamoorthy Bhuvanendran [a], Sabarinathan Ravichandran [a], Sabariswaran Kandasamy [a], Weiqi Zhang [a], Qian Xu [a,**], Lindiwe Khotseng [b], Thandavarayan Maiyalagan [c], Huaneng Su [a,*]

[a] _Institute for Energy Research, Jiangsu University, 301 Xuefu Road, Zhenjiang, 212013, PR China_
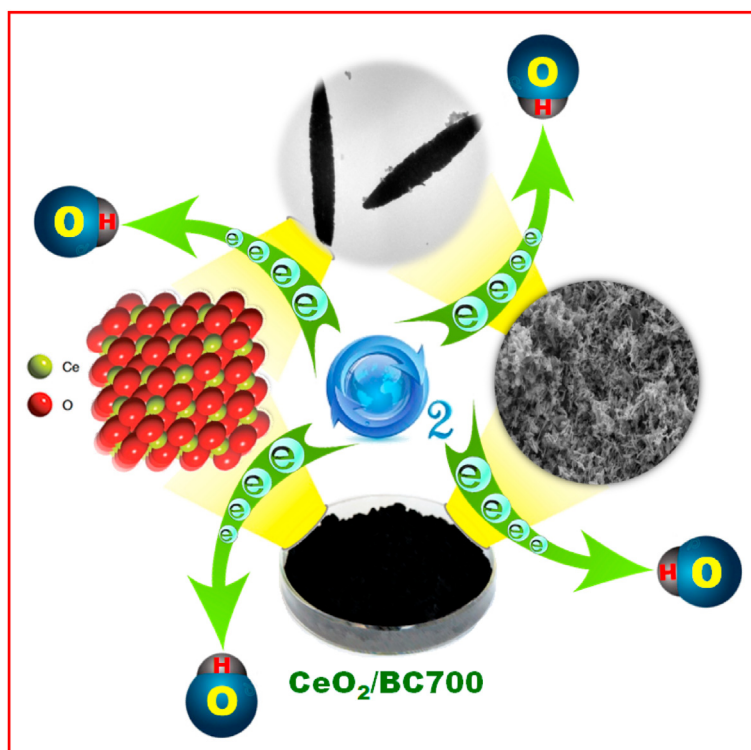[b] _Department of Chemistry, University of the Western Cape, Cape Town, 7535, South Africa_
[c] _Department of Chemistry, SRM Institute of Science and Technology, Kattankulathur, 603203, Tamilnadu, India_

HIGHLIGHTS

- Spindle-shaped CeO₂ on bio-char carbon synthesized by _in-situ_ hydrothermal method.
- Naturally occurring _Spirulina platensis_ microalgae used as the carbon source.
- N, P - doped carbon and O-vacancy of Ce³⁺ in CeO₂/BC700 promote the ORR kinetics.
- CeO₂/BC700 has good ORR activity and remarkable stability after 5000 cycles.

GRAPHICAL ABSTRACT

ABSTRACT

Highly durable and active CeO_2 on biochar carbon (CeO_2/BC) derived from *Spirulina platensis* microalgae and synthesized by simple one-pot hydrothermal treatment and further activated through pyrolysis approach. A spindle-shaped morphology of CeO_2 with predominant (111) facet was evidently observed from X-ray diffraction patterns and electron microscopy images. The structural features such as high specific surface area, defect-rich carbon with N & P atoms, increased oxygen vacancy and π-electron transfer play an important role for the improved oxygen reduction reaction (ORR). The considerable amount of Ce^{3+} and higher proportion of pyridinic N and graphitic N species are substantially contributed to the superior ORR performance of CeO_2/BC700, which surpasses other similar catalysts and competing with Pt/C. Hence, the significant kinetic ORR parameters and extended stability (no loss after 5000 potential cycles) of the CeO_2/BC700 catalysts provides the promising insight to develop the rare-earth metal oxide nanostructures as a possible candidate for ORR in alkaline medium.

© 2020 Hydrogen Energy Publications LLC. Published by Elsevier Ltd. All rights reserved.

Introduction

A rational design and development of electrocatalysts towards oxygen reduction reaction (ORR) could be a vital electrode process of sustainable energy conversion and storage technologies [1–3]. Although, the low temperature fuel cells (LTFCs) turned as an emerging clean energy conversion device, the slow kinetics and complex reaction mechanism of ORR restricting the overall performance [4–6]. The Pt and Pt-based catalysts are widely recognized and employed as the prime choice of electrocatalyst for ORR [7,8]. The high cost, less abundance and poor stability of Pt based electrocatalysts are critically impacting the commercial viability. Hence, significant attentions were paid to find the suitable electrocatalysts with improved ORR activity and stability for LTFCs [9–11]. However, it remains a critical task for researchers to explore the active catalysts with cost-effective measures for large-scale applications.

Moreover, the non-noble metal catalysts such as metal oxides, perovskites, spinel oxides, metal oxy-hydroxides and metal organic frameworks with various carbon supports have been extensively studied for ORR in alkaline medium [10,12,13]. Notably, the rare-earth metal oxide of ceria (cerium oxide, CeO_2) was found as a potential choice of electrocatalyst featuring excellent chemical stability, oxygen storage ability, facile electron transfer (Ce^{4+}/Ce^{3+} redox couple) and relatively low-cost [14,15]. It has been widely employed as the effective catalyst and co-catalyst/promoter with another noble and non-noble metals in electrocatalysis for various energy conversion and storage applications [16–18]. Interestingly, the Ce^{4+}/Ce^{3+} redox couple feature as an efficient oxygen buffer during the electrochemical oxidation/reduction reactions, where it can able to release and adsorb/store the oxygen depending on the nature of the reaction. This classical property of ceria could be a crucial part of the enriched oxygen vacancy which induces the improved mechanical and electrochemical stability [19,20].

Recent literatures demonstrate that, the unique redox property of ceria makes it an active co-catalyst with Pt, such as $Pt–CeO_2@CN$ [21], $Pt–CeO_2@C$ [22], $Pt-CeO_x/C$ [23], $Pt–CeO_2/rGO$ [21] and unsupported $Pt–CeO_2$ [24] for ORR in both acid and alkaline electrolytes. Some of the literatures have reported the non-platinum catalysts with CeO_2, such as Ag decorated CeO_2 [25], PdCo-Ceria [26], Ceria@Co–N–PCN [27], $CeO_2/Co_3O_4@NC$ [28], $Co–CeO_2–N–C$ [29], $Co_3O_4–CeO_2/KB$ [30], $CeO_2/CePO_4@N$, P co-doped carbon [31], $CeO_2/Co@N$-doped carbon [32], Ce/Fe–NCNW [33] and $Mn–CeO_2/rGO$ [34] showing decent ORR activity owing to the synergistic effect between CeO_2 and other metal catalysts. However, few investigations were reported on the CeO_2 as single active catalyst for ORR in alkaline medium. Sun et al. studied the electrocatalytic performance of CeO_2/rGO nanocomposite prepared through mild ultrasonic-reflux method for oxygen reduction and oxygen evolution reactions. They conclude that, the strong coupling effect between rGO and CeO_2 contributed the improved oxygen bifunctional performance in KOH medium [35]. The effect of synthesis approach and the composition of CeO_2 with carbon have been investigated for electrogeneration of hydrogen peroxide (H_2O_2), reported by Assumpcao et al. They found that the 4% CeO_2 as the optimal loading on a carbon with 88% of H_2O_2 production and follows nearly 2-electron reduction pathway [36].

Soren et al. [15] prepared the nano ceria supported NrGO catalyst by a single step solvothermal method. They found the kinetic current density (j_k) of 9.5 mA/cm² for $CeO_2/NrGO$, which implies the improved methanol tolerance and ORR activity owing to the effective interaction of catalytic materials. In another work, they reported CeO_2 embedded on graphitized-Carbon nitride (g-C_3N_4) prepared by microwave-assisted solvothermal approach. The resulted CeO_2/g-C_3N_4 showed considerable ORR activity with the average number of electrons transferred as 3.2, due to the key role of pyridinic nitrogen from g-C_3N_4 acting as a promoter of ORR [37]. Peng et al. [38] reported the in-situ growth of CeO_2 on rGO through the controlled heat treatment under inert atmosphere. The

intrinsic ORR activity of CeO_2-rGO750 was found to be superior to standard Pt/C catalysts with a higher j_k value (20.31 mA cm^{-2}). It is well known that the existence of heteroatoms (N, P, S and B) in carbon materials have a modified electronic and chemical properties than pure carbon materials [14,39]. Hence, the heteroatoms can alter the electronic distribution of the carbon frameworks which effectively increasing the π-electron transfer to balance the electroneutrality of carbon atoms. In addition, the synergistic effect between the carbon and heteroatoms can be more favorable for oxygen adsorption and reduction (oxygen bond breaking), which concurrently promote the electrocatalytic performance of the materials for improved ORR [14,40].

These literatures clearly demonstrated that, the carbon supported CeO_2 (CeO_2/C) nanostructures could be employed as an efficient ORR catalyst with induced interaction (strong coupling) and synergistic effect between the catalyst components. But, the stability factor of the catalysts has not been well-studied and that should be addressed without compromising the ORR catalytic activity. Based on the above literatures, we are inspired to prepare the CeO_2/C catalyst with strong coupling effect, synergistic effect and extend durability through specific choice of carbon source and a simple synthesis method.

Herein, we report the in-situ preparation method for the spindle-shaped CeO_2 nanostructures supported on biochar derived carbon (BC). A 'Spirulina platensis' microalgae (SPM), which can be found in both fresh water and marine [41], was used as the carbon source. It is a potential bio-energy material readily available as a natural source, which contains self-doped N and P elements. The CeO_2/BC was further activated by pyrolysis treatment under N_2 atmosphere and used as the electrocatalyst for ORR in KOH medium. The morphological features and elemental composition of CeO_2/BC were studied thoroughly by the essential surface characterization techniques. The defect-rich mesoporous structure of BC with a higher proportion of graphitic N and pyridinic N were proposed to be one of the favorable ORR active sites. The bio-inspired carbon source (SPM) with oxygen defect-rich CeO_2 nanostructure, which can provide more active key components to promote the kinetics of ORR, could be the interesting aspect of this present study. Hence, the electrocatalytic activity and stability of CeO_2/BC were comparatively superior to other reported CeO_2-based catalysts and competing with standard 20% Pt/C.

Experimental methods

Preparation of biochar derived carbon (BC)

The carbon source of SPM was purchased from Guangxi Nongken Green Fairy Health Food Co. Ltd., China. 5 g of pre-heated SPM was dispersed in 100 mL ultrapure (UP) water under ultra-sonication for 30 min to obtain homogenous distribution. The solution was poured into the Teflon-lined stainless-steel autoclave reactor, at 160 °C heating for 12 h. Then, the hydrothermal biochar (BC) treated by mixing of 0.1 M HCl solution under vigorous stirring for 3 h. The final product was washed with copious amount of Millipore water

(18 MΩ cm) by centrifugation (8000 rpm) until the pH of the supernatant solution reaches the neutral. Finally, the brown-black colored BC powder was obtained by drying at 90 °C in air-oven for 6 h. This BC was further activated through pyrolysis at 700 °C at the rate of 5 °C min^{-1} for 2 h under N_2 atmosphere.

Preparation of BC supported spindle shaped cerium oxide (CeO_2/BC) nanostructures

The CeO_2/BC catalyst was prepared by one-pot hydrothermal method as follows (Fig. 1). Nine grams of cerium (III) nitrate hexahydrate ($Ce(NO_3)_3.6H_2O$, Sigma Aldrich), 7.2 g of urea ($CO(NH_2)_2$, Sigma Aldrich) and 1.2 g of polyvinylpyrrolidone-40000 (PVP40, Sigma Aldrich) mixed together in 150 mL of Millipore water through ultra-sonication. In this transparent mixture, 8 g of pre-heated SPM was dispersed and stirred for 1 h for homogeneous condition. Then, the above mixture was carefully transferred into the hydrothermal reactor (250 mL, autoclave reactor) and heated at 160 °C for 12 h in hot air-oven. The gray-black slurry was obtained through high-speed centrifugation (10,000 rpm) and washed thoroughly with water/ethanol mixture to eliminate the impurities. The moisture content of CeO_2/BC was removed by heating at 90 °C for 6 h and used for pyrolysis treatment. The CeO_2/BC catalyst was further activated by pyrolysis approach at different temperatures (700, 800 and 900 °C) using tubular furnace for 2 h at the rate of 5 °C min^{-1} under N_2 gas flow and the catalysts are named after the respective pyrolysis temperature. For comparison, the standard carbon supported platinum nanoparticles (20% Pt/C) was prepared thru a simple chemical reduction approach with formaldehyde at elevated temperature (120 °C for 6 h). The average Pt nanoparticle size was found between 2 and 3 nm, reported in our previous article [42].

Characterization techniques

The structural features of the catalytic materials were studied using field-emission scanning electron microscopy (FESEM, JSM-7800F) and high-resolution transmission electron microscopy (TEM, JEM-2100, JEOL) techniques. The porosity and specific surface area were found by Brunauer-Emmett-teller (BET, Tristar II 3020) analysis. The nature of carbon and its surface defects were analyzed by using Raman spectra (DXR, ThermoFisher). The elemental oxidation state and composition were estimated by X-ray photoelectron spectroscopy (XPS, ESCA LAB 250Xi) and the bulk composition was obtained from the energy dispersive X-ray spectroscopy (EDX-mapping) technique. The crystallographic properties were examined by using powder X-ray diffractometer (XRD-6100) with the $\lambda = 1.54$ Å at 30 kV.

The cyclic voltammetry (CV) and polarization (linear sweep voltammetry, LSV) curves were recorded using the electro-chemical workstation (CHI 760E) coupled three-electrode system equipped with a working electrode of rotating ring-disc electrode (RRDE, Pt (0.1866 cm^2)-GC (0.2475 cm^2)). The Ag/AgCl and a thin Pt wire or a graphite rod were employed as the reference and counter electrode respectively. For the preparation of catalyst ink, 5 mg of catalyst in 1 mL of Ethanol and 20 μL Nafion (5 wt % alcohol solution) were mixed under
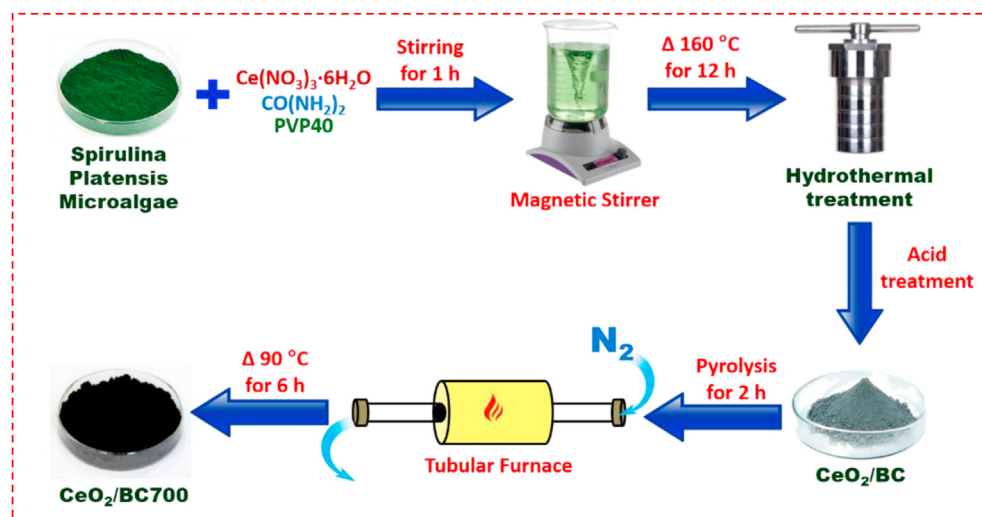
Fig. 1 – Graphical representation for the synthesis of CeO₂/BC700 catalyst.

ultra-sonication for 10 min. Exactly, 10 μL of fresh catalyst ink was drop-casted over the working electrode (GC surface) and dried under ambient conditions. The final catalyst loading was about 80 μg cm^{-2} over the electrode.

To probe the ORR electrocatalytic activity of the catalysts, the CV and LSV profiles were obtained in 0.1 M KOH under high pure N_2 and O_2 atmosphere. The hydrodynamic LSV executed between 400 and 2400 rpm at 0.01 V s^{-1}. Here, the potential was reported against reversible hydrogen electrode (RHE) and all the electrochemical studies carried out at 25 °C. During RRDE-LSV studies, the ring potential was fixed at 1.2 V vs. RHE. The stability test was performed through the potential cycling (PC) between 0.6 and 1.1 V vs. RHE at 0.1 V s^{-1} under static condition. At regular intervals, LSV curve was recorded at 1600 rpm up to a maximum of 5000 PCs.

Results and discussion

The crystalline phases of CeO₂/BC catalysts were examined by XRD patterns, as presented in Fig. 2a. All the three CeO₂/BC (700, 800 and 900) catalysts show distinct diffraction peaks located at nearly 28.4°, 32.9°, 47.4°, 56.2°, 59.0°, 69.3°, 76.6°, 78.9° and 88.3° corresponds to (111), (200), (220), (311), (222), (400), (331), (420) and (422) facets respectively [43]. These cubic crystalline phases are clearly indicating the fluorite lattice structure of CeO₂, which is a good match with the reported literatures and JCPDS data file no. 43–1002 [43–45]. The sharp and well intense diffraction peaks with no other phases suggest a good crystalline behavior and high purity of the CeO₂ nanostructures.

The predominant (111) diffraction peak is considered as the most stable crystalline facet of CeO₂ [46]. The d-spacing values were calculated using Eq. (1), about to be 0.3138 nm, 0.3133 nm and 0.3128 nm for CeO₂/BC700, CeO₂/BC800 and CeO₂/BC900 respectively. Moreover, the surface defects and oxygen vacancies are highly relevant to the crystalline phase and dominating the catalytic behavior. The lattice parameters (*a*)

determined by Eq. (2), could be a significant measure to probe the oxygen vacancy [47,48].

$$d = \frac{n\lambda}{2\sin\theta} \tag{1}$$

$$a = d_{hkl}\left(\sqrt{h^2 + k^2 + l^2}\right) \tag{2}$$

Here, *n* is an integer (n = 1), λ is the wavelength (1.53 Å), θ is the diffraction angle, *hkl* are the miller indices. The order of '*a*' found as 5.4351 Å (CeO₂/BC700)> 5.4265 Å (CeO₂/BC800)> 5.4178 Å (CeO₂/BC700). Thus, the higher lattice parameter value for CeO₂/BC700 indicates the lattice expansion due to high concentration of Ce^{3+} surface defects [49]. Whereas, the XRD pattern for BC was observed with the broad peak around 23–26° and 43.1° that assigned to (002) and (100) facets, indicating the graphite structure of carbon support [50,51]. These peaks were not noticeable in all the three CeO₂/BC catalysts due to the high intensity CeO₂ diffraction planes.

Fig. 2b shows the N_2-adsorption/desorption isotherms for BC and all other three CeO₂/BC (700, 800 and 900) catalysts. These profiles are observed as a typical type-IV characteristic isotherms elucidating the mesoporous structure of the materials. The higher specific surface area obtained from BET was about 135.88 m^2 g^{-1} for CeO₂/BC700 compared to CeO₂/BC800 (115.44 m^2 g^{-1}), CeO₂/BC900 (74.13 m^2 g^{-1}) and BC (98.14 m^2 g^{-1}). The higher specific surface area and mesoporous structure of CeO₂/BC700 could contribute to the improved ORR performance by having more active sites with efficient mass transport of oxygen species [14]. The pore size distribution was determined from the respective desorption isotherms by BJH and given in Fig. S1. This size range clearly indicates that the mesoporosity of the BC supported CeO₂ catalysts, which has minimal impact over the pore size distribution. The mean pore diameter of BC was about 3.1 nm and for CeO₂/BC700, 800 and 900 catalysts were between 3.7 and 3.8 nm. Raman spectra was performed to determine the graphitic (G) and defective (D) characteristics of carbon support as shown in Fig. 2c. In addition to that, the concentration of oxygen vacancies in CeO₂/BC was calculated and
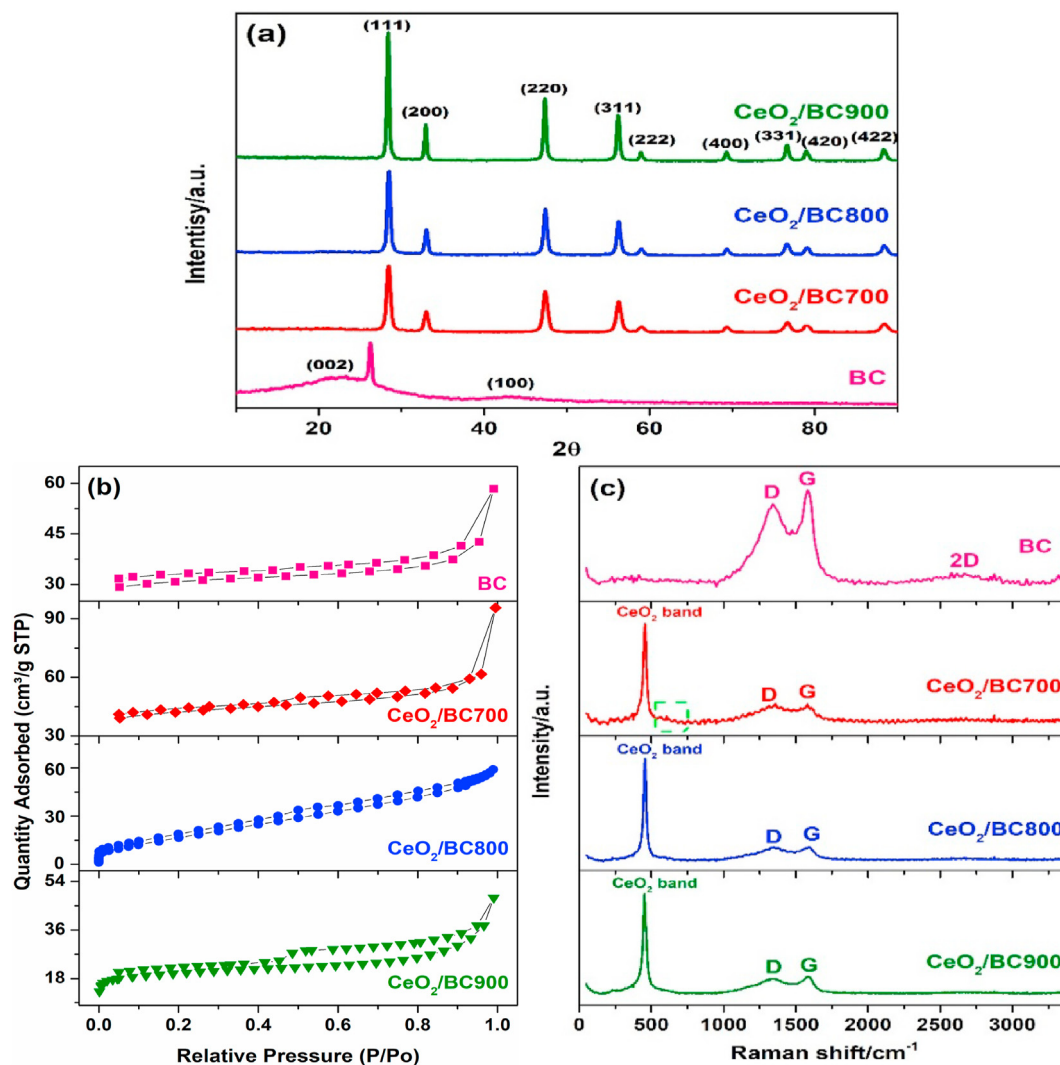
Fig. 2 — (a) Powder XRD patterns, (b) Nitrogen adsorption/desorption isotherms and (c) Raman spectra for BC, CeO$_2$/BC700, CeO$_2$/BC800 and CeO$_2$/BC900 catalysts.

considered as the catalytic activity descriptor as mentioned in the previously reported literatures [52–54].

Both BC and CeO$_2$/BC (700, 800 and 900) catalysts show distinct peaks at ~1340 and 1582 cm^{-1} assigned to 'D' and 'G' carbon bands. Whereas, the ratio of peak intensity (I_D/I_G) was found as 0.84, 1.1, 1.0 and 0.84 for BC, CeO$_2$/BC700, CeO$_2$/BC800 and CeO$_2$/BC900 respectively. The amount of defective sites found higher for CeO$_2$/BC700 clearly indicates that the carbon support has disordered graphite structure [55]. This phenomenon was well in agreement with the XRD results. A sharp and intense peak was observed at around 455 cm^{-1} representing to the F$_2$g level of CeO$_2$ fluorite phase in all the three CeO$_2$/BC catalysts. Whereas, the less intense peak observed at ~596 cm^{-1} for CeO$_2$/BC700 (highlighted with a green box in Fig. 2c) is associated with vacant oxygen sites, which was well correlated with XPS results for the higher surface oxygen vacancies [49] compared to other catalysts as the latter showed no similar peaks.

The surface chemical state and elemental composition was studied using XPS analysis and the survey spectra (Fig. S2a) of

CeO$_2$/BC700 catalyst depicts the series of peaks corresponding to Ce 3d, N 1s, C 1s, P 2p and O 1s elements. The elemental composition of CeO$_2$/BC700 catalyst was about (atomic weight %) 14.42% Ce, 2.04% N, 17.8% O, 0.23% P and 65.51% C. The deconvoluted Ce 3d spectra was presented in Fig. 3a with two peak series of 3d$_{3/2}$ and 3d$_{5/2}$ representing both Ce^{4+} and Ce^{3+} oxidation states. The spin-orbit splitting peaks were located at the binding energies of 898.3 eV, 900.9 eV, 907.4 eV and 916.8 eV belongs to 3d$_{3/2}$, and the peaks at 882.4 eV and 888.7 eV for 3d$_{5/2}$ attributes to Ce^{4+} oxidation state [35]. Whereas, the weak satellite peaks were observed at 885.2 eV and 903.7 eV corresponding to Ce^{3+} oxidation state confirming the redox behavior of CeO$_2$ that could facilitate the increase of oxygen concentration on the catalyst surface [14,54]. Hence, the Ce^{3+} content in CeO$_2$/BC700 catalyst may contribute to generate the oxygen vacancy and increase the adsorption/ storage capability on the catalyst surface. The intrinsic oxygen vacancy is more favorable for improved oxygen mass transport and determine the enhanced electrocatalytic performance towards ORR [14,19,56].
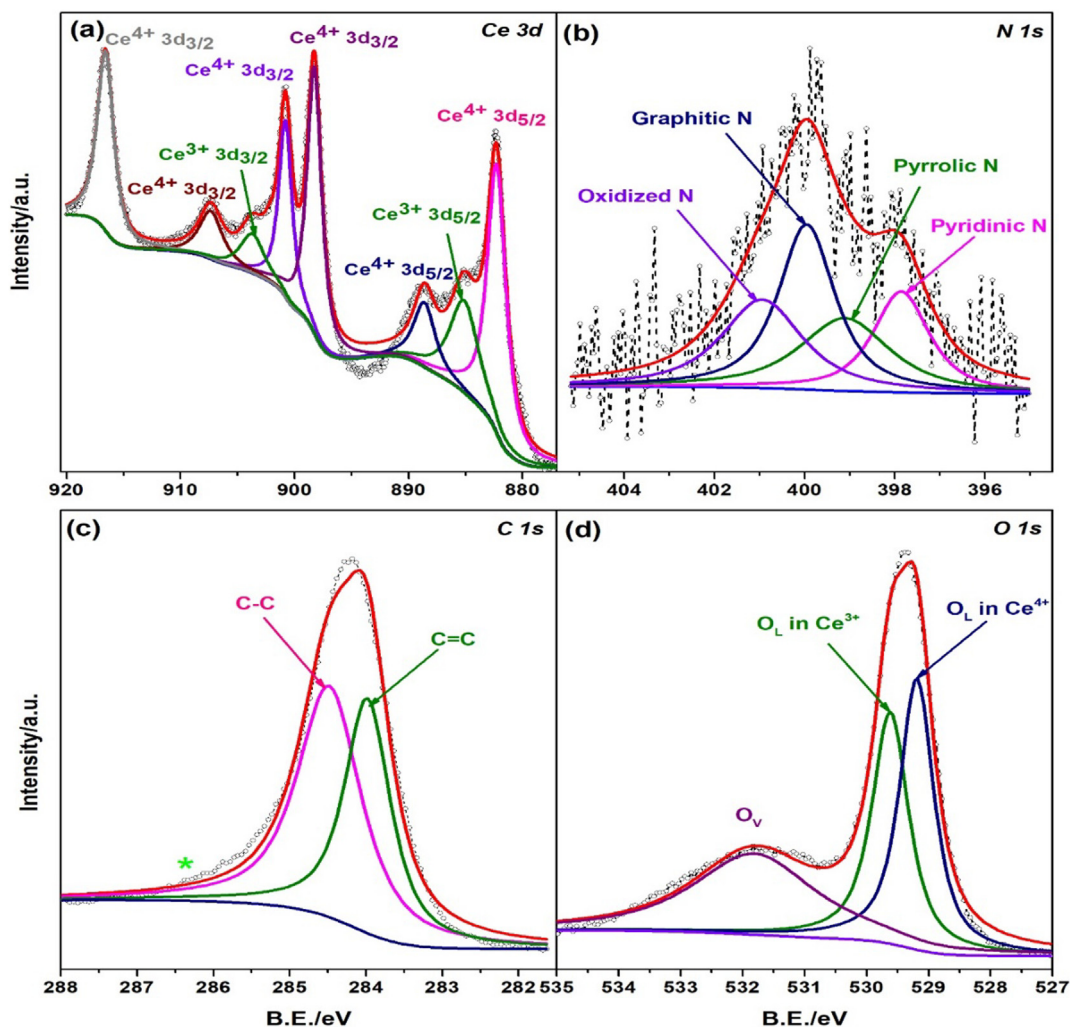
Fig. 3 – Deconvoluted XPS peaks of (a) Ce 3d, (b) N 1s, (c) C 1s and (d) O 1s for CeO_2/BC700 catalyst.

The XPS spectra of N 1s (Fig. 3b) were deconvoluted into four characteristic peaks of nitrogen assigned to pyridinic N (398.1 eV), pyrrolic N (399.1 eV), graphitic N (399.9 eV) and oxidized N (400.9 eV), which are believed to play significant roles on ORR activity [3,57]. Hence, the graphitic N (39%) and pyridinic N (22.7%) has the major proportion than pyrrolic N (16.7%) and oxidized N (21.6%) species, which may contribute to the good ORR catalytic performance of CeO_2/BC700 [14,58]. Fig. 3c shows the C 1s spectra fitted into two distinct peaks at 283.9 eV and 284.5 eV associated with the sp^3 and sp^2 hybridized carbon (C–C) and (C=C) respectively. An un-deconvoluted satellite peak (denoted by *) appeared at ~285.9 eV could be attributed to the C–N, implying the possible delocalization of π-electrons between nitrogen and carbon atoms [14,59]. The peak fittings for O 1s spectra (Fig. 3d) show two distinct forms of oxygen species designated as the doublet of lattice oxygen (O_L) at 529.2 eV for Ce^{4+} and 529.6 eV for Ce^{3+} with the vacant oxygen (O_V) at 531.8 eV. This phenomenon was in well agreement with Ce^{3+} content in CeO_2/BC700, implying the increased oxygen vacancy at the catalyst surface may account for the enhancement of ORR performance [60,61]. Whereas, the P 2p spectra (Fig. S2b) shows an

undistinguished but a considerable peak observed at around 132.9 eV corresponding to P–C bonding [62], which could be the substantial evidence of phosphorous interaction at the carbon skeleton.

The spindle-like morphology of CeO_2 was clearly observed from the FESEM images provided in Fig. S3 for all the three CeO_2/BC (700, 800 and 900 °C) catalysts. The length of the CeO_2 spindle was about ~7–9 μm and the diameter found between 700 nm and 1 μm. Moreover, the spindle shape of CeO_2 changed into irregular morphology for the catalysts at higher pyrolysis temperatures of 800 and 900 °C (Figs. S3a–c). Fig. 4a–f shows the FESEM elemental mapping for each element (inset of table in Fig. 4g) present in the catalytic material and confirm the existence of self-doped N, P elements with uniform distribution throughout the sample. Whereas, the elemental composition of CeO_2/BC700 catalyst was evaluated by using EDX analysis and it showed similar values for all elements in atomic weight % as obtained from the XPS analysis.

Fig. 5a and b shows the TEM images of BC with porous morphology and no evidence for the crystalline nature of the carbon was observed from selected-area electron diffraction
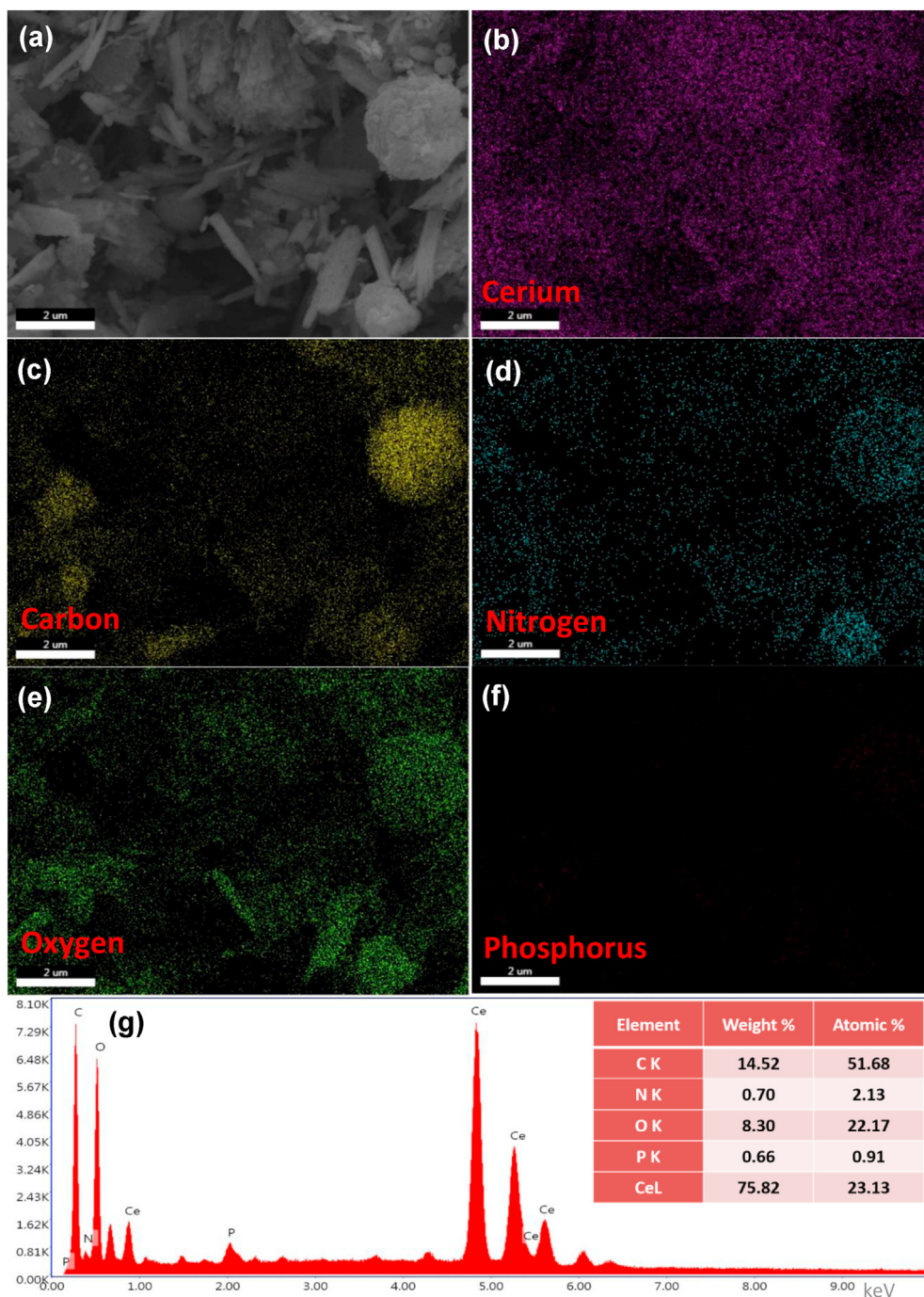
Fig. 4 − (a−f) FESEM elemental mapping and (g) EDX analysis of CeO$_2$/BC700 catalyst.

(SAED) pattern (inset of Fig. 5b). This phenomenon was well consistent with the Raman results of BC. For CeO$_2$/BC700, the TEM image represents the well-defined structure of spindle-shaped CeO$_2$ with sharp edges and distinct boundaries with carbon layers for as given in Fig. 5c. However, the shape of CeO$_2$ was found deformed at the edges for CeO$_2$/BC800 (Fig. 5e) and CeO$_2$/BC900 (Fig. 5g), which might be resulted from the higher pyrolysis temperature. From the HRTEM images (Fig. 5d, f and 5h), the interplanar distance (*d*-spacing) of crystalline fringes about 0.313 nm corresponding to fluorite structure of CeO$_2$ with the growth of (111) crystalline

orientation. The SAED pattern for CeO$_2$/BC700 (inset of Fig. 5d) presents ordered orientation with (111) facet as the predominant crystalline plane. The high temperature pyrolysis catalysts (CeO$_2$/BC800, inset of Fig. 5f and CeO$_2$/BC900, inset of Fig. 5h) show the disordered arrangement of crystalline orientation, which further confirms the effect of pyrolysis temperatures.

The ORR electrocatalytic performance of BC and CeO$_2$/BC (700, 800 and 900 °C) catalysts was studied in KOH medium at 25 °C. Fig. 6a depicts the CV profiles recorded in both N$_2$ and O$_2$ purged at 0.1 V s^{-1} for all the catalytic materials. Among the
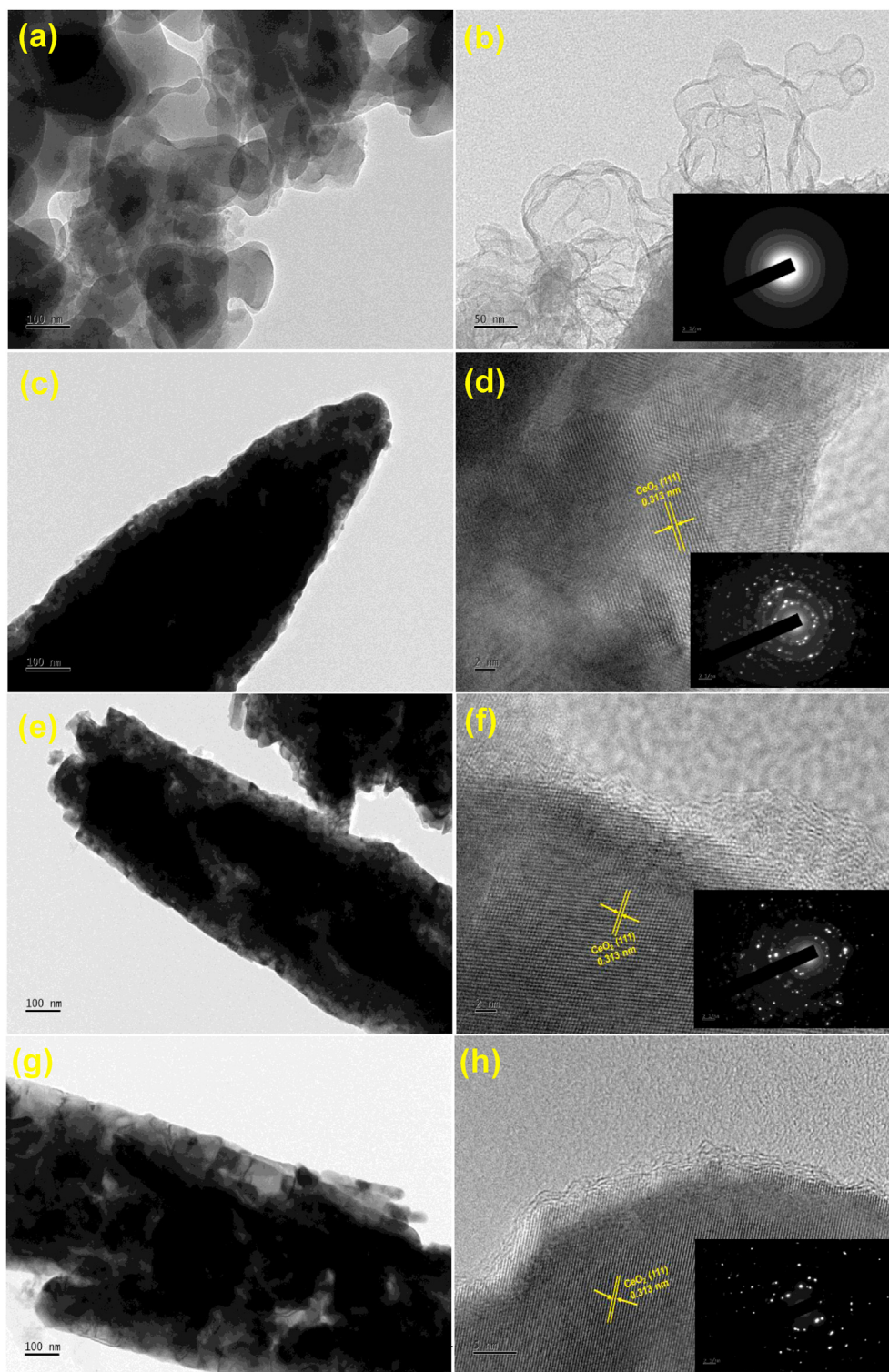
Fig. 5 – TEM & HRTEM images of (a & b) BC, (c & d) CeO$_2$/BC700, (e & f) CeO$_2$/BC800 and (g & h) CeO$_2$/BC900 catalysts (Inset: SAED patterns of the respective catalysts).

catalytic materials, CeO$_2$/BC700 showed prominent redox peaks between 0.0 and 0.5 V vs. RHE under N$_2$ atmosphere, which might be due to the formation of surface oxygen functionalities and no such distinct behavior was observed for other catalysts, including BC. This could be due to the surface functional defects may induce the surface oxygen defects

(vacancy) on the electrode materials, which is more favorable for the improved ORR kinetics as reported in many literatures [63]. At the O$_2$ saturated conditions, a well pronounced oxide reduction peak was observed and that could be the sign of catalytic ability of all the catalysts for ORR [47]. The onset potential (E_{on}) from the respective CV showed an order of BC
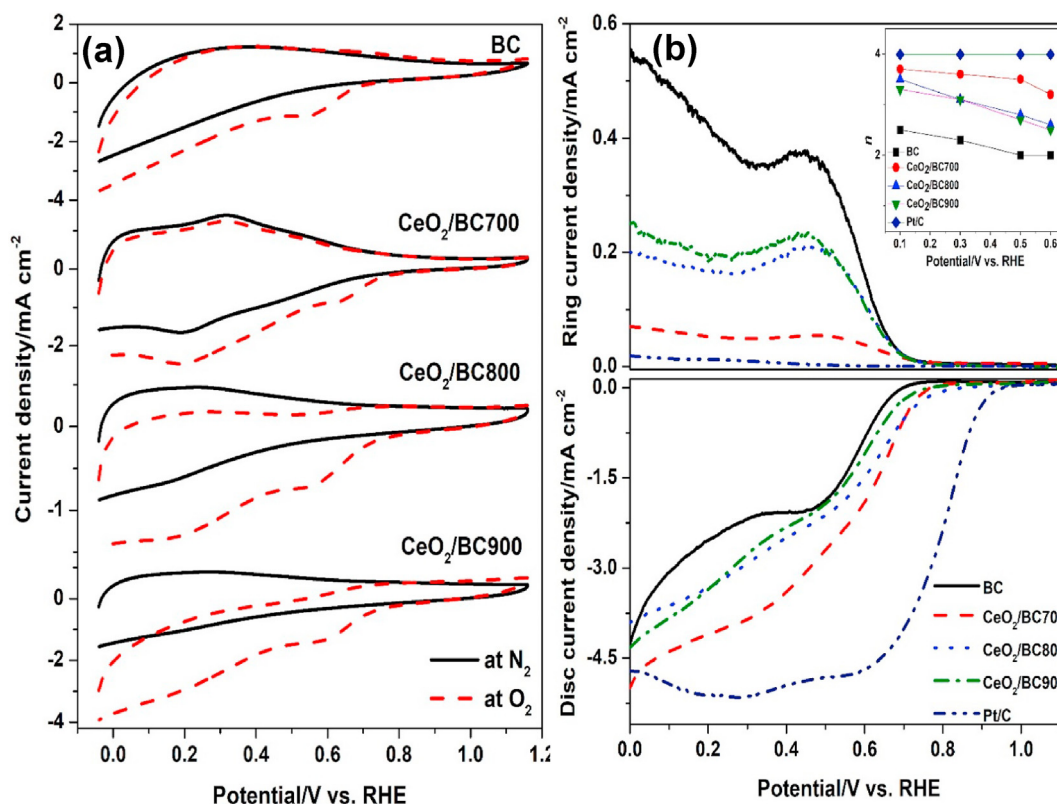
Fig. 6 – (a) CVs and (b) RRDE-LSV profiles for BC, CeO$_2$/BC700, CeO$_2$/BC800 and CeO$_2$/BC900 catalysts compared with Pt/C in N$_2$ and O$_2$ saturated 0.1 M KOH at a scan rate of 0.1 V s^{-1} and 0.01 V s^{-1} at 1600 rpm. (Inset: no. of electrons transferred as a function of potential from RRDE test).

(0.71 V) < CeO$_2$/BC900 (0.76 V) < CeO$_2$/BC800 (0.77 V) < CeO$_2$/BC700 (0.79 V), this could be the significant indication for the improved ORR performance on CeO$_2$/BC700 catalyst. In order to calculate the electrochemical active surface area (ECSA) of the catalysts, the specific capacitance was determined from the respective CV profiles by adapting the following Eq. (3) [64].

$$A_{ECSA} = \frac{specific\ capacitance}{40\ \mu F/cm^2\ per\ cm^2_{ECSA}} \qquad (3)$$

where, the specific capacitance for a flat surface of the electrode found between 20 and 60 μF cm^{-2}, we have taken a moderate value of 40 μF cm^{-2} for the ECSA calculation. Hence, the ECSA values are found as 0.0274, 0.0210, 0.0089 and 0.0053 cm^2 for CeO$_2$/BC700, CeO$_2$/BC800, CeO$_2$/BC900 and BC catalysts. This clearly indicates that the CeO$_2$/BC700 possess better active surface compared to other catalysts.

Fig. 6b compares, the ORR polarization curves (RRDE-LSV) of BC, CeO$_2$/BC (700, 800 and 900 °C) with Pt/C as reference catalyst at O$_2$ saturated 0.1 M KOH at 0.01 V s^{-1} under hydrodynamic conditions. The earlier onset potential (E_{on}, 0.79 V), half-wave potential ($E_{1/2}$, 0.60 V) and higher disc current density (j, 4.4 mA cm^{-2} at 0.1 V) of CeO$_2$/BC700 catalyst indicates greater ORR activity than other catalysts. Moreover, the Pt/C shows ~160 mV more positive E_{on} value than that of CeO$_2$/BC700, but their ORR limiting current densities were similar (4.8 vs. 4.4 mA cm^{-2}) with each other. Amongst, the CeO$_2$/BC700 showed lowest ring current density and the

number of electrons transferred (n) during ORR was about 3.1–3.7 at the potential range 0.1–0.6 V.

For BC, CeO$_2$/BC800 and CeO$_2$/BC900 catalysts, the 'n' values were found between 1.5 and 3.0, which was expected to follow 2-electron transfer pathway for ORR. This result clearly suggests (inset of Fig. 6b) that the ORR on CeO$_2$/BC700 follows nearly the 4-electron transfer pathway as processed on Pt/C (n = 3.9–4.0). In addition to this, the percentage of HO$_2^-$ was evaluated based on the ring (I_R) and disc (I_D) current values at 0.1–0.6 V (Fig. S4) using the following Eq. (4) [37],

$$\%HO_2^- = \frac{200\left(\frac{I_R}{N}\right)}{I_D + \left(\frac{I_R}{N}\right)} \qquad (4)$$

where, N is the collection efficiency of the RRDE (N = 38%, as mentioned by the manufacturer). The %HO$_2^-$ increases in the order of CeO$_2$/BC700 (11.7%) < CeO$_2$/BC800 (43.1%) < CeO$_2$/BC900 (48.6%) < BC (70.8%) at 0.6 V, which has a good agreement with the n values and compared to other carbon supported CeO$_2$ based catalysts from literature reports [34,37].

Furthermore, the kinetics of ORR were determined by using the Koutecky-Levich (K-L) plot $\left(\frac{1}{j}\ vs.\ \frac{1}{\omega^{1/2}}\right)$ for the respective catalysts and presented in Fig. 7a–e. From the K-L slope, the 'n' values are estimated using the K-L Eqs (5), (6) & (7) as rearranged below [3,65,66].
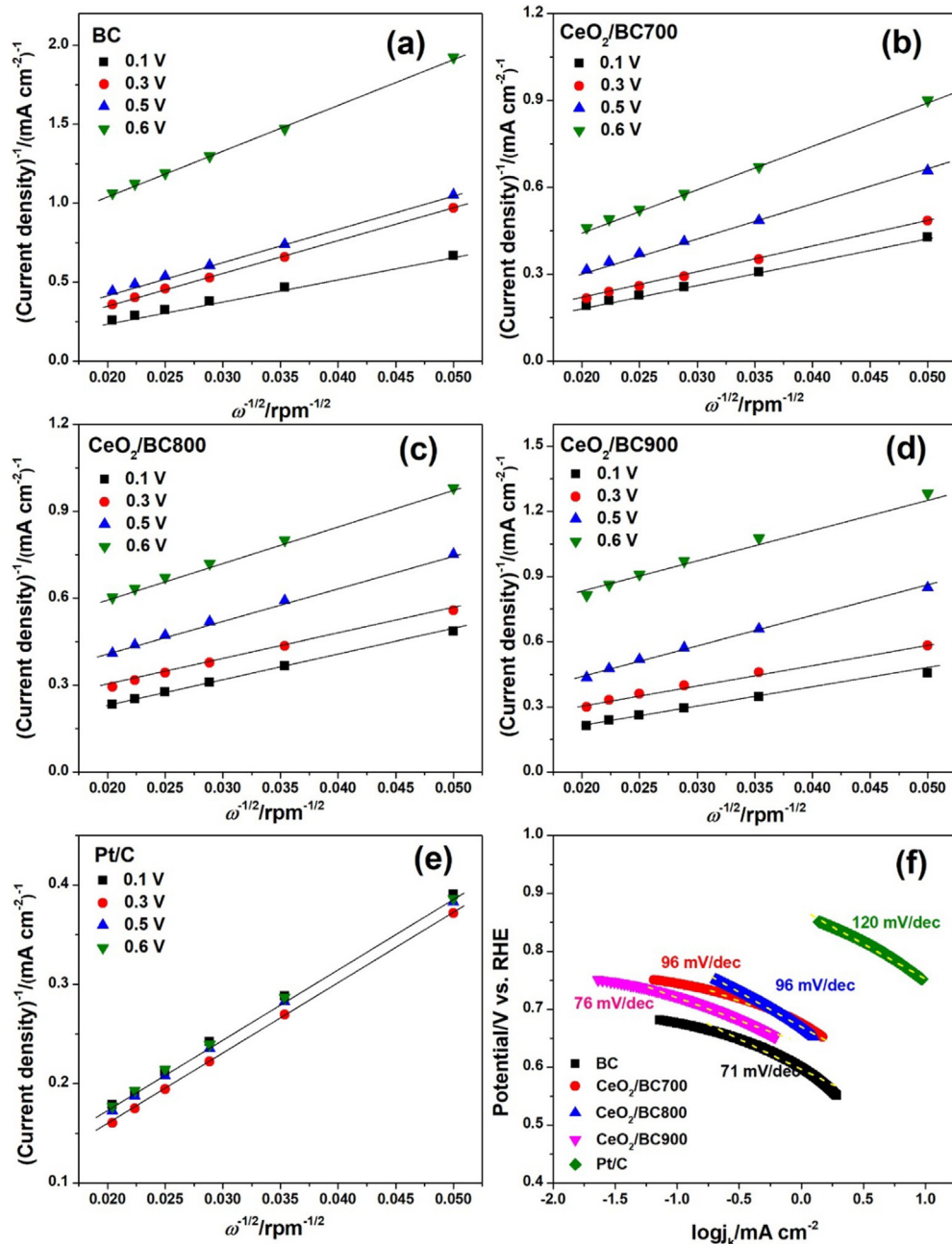
Fig. 7 – (a–e) K-L plots at different potentials and (f) Tafel plots for BC, CeO$_2$/BC700, CeO$_2$/BC800 and CeO$_2$/BC900 catalysts compared with Pt/C.

$$\frac{1}{j} = \frac{1}{j_k} + \frac{1}{B\omega^{1/2}} \quad (5)$$

$$B = 0.2nF\left(D_{O_2}\right)^{2/3}\nu^{-1/6}C_{O_2} \quad (6)$$

$$n = \frac{B}{0.2F\left(D_{O_2}\right)^{2/2}\nu^{-1/6}C_{O_2}} \quad (7)$$

Here, 'j' is the disc current density (mA cm^{-2}) at 0.1 V, j$_k$ is the kinetic current density (mA cm^{-2}), B is the K-L slope value, ω is the electrode rotation rate (rpm), F is Faraday's constant

(96,500C mol^{-1}), C$_{O2}$ is the concentration of oxygen (1.2 × 10^{-3} mol/L), D$_{O2}$ is the oxygen diffusion coefficient (1.9 × 10^{-5} cm^2 s^{-1}) and ν is the kinematic viscosity (1 × 10^{-2} m^2 s^{-1}) [37].

The K-L plots are found nearly parallel and linear at 0.1–0.6 V for both BC and CeO$_2$/BC (700, 800 and 900 °C). The calculated 'n' values are of ~3.3–3.7 for CeO$_2$/BC700, comparable to Pt/C (3.9–4.0) and better than CeO$_2$/BC800 (2.0–3.1), CeO$_2$/BC900 (2.0–3.0) and BC (1.5–2.1). This phenomenon clearly suggests that the ORR on CeO$_2$/BC700 follows near 4-electron reduction pathway with first-order reaction kinetics and the first electron transfer step considered as the rate
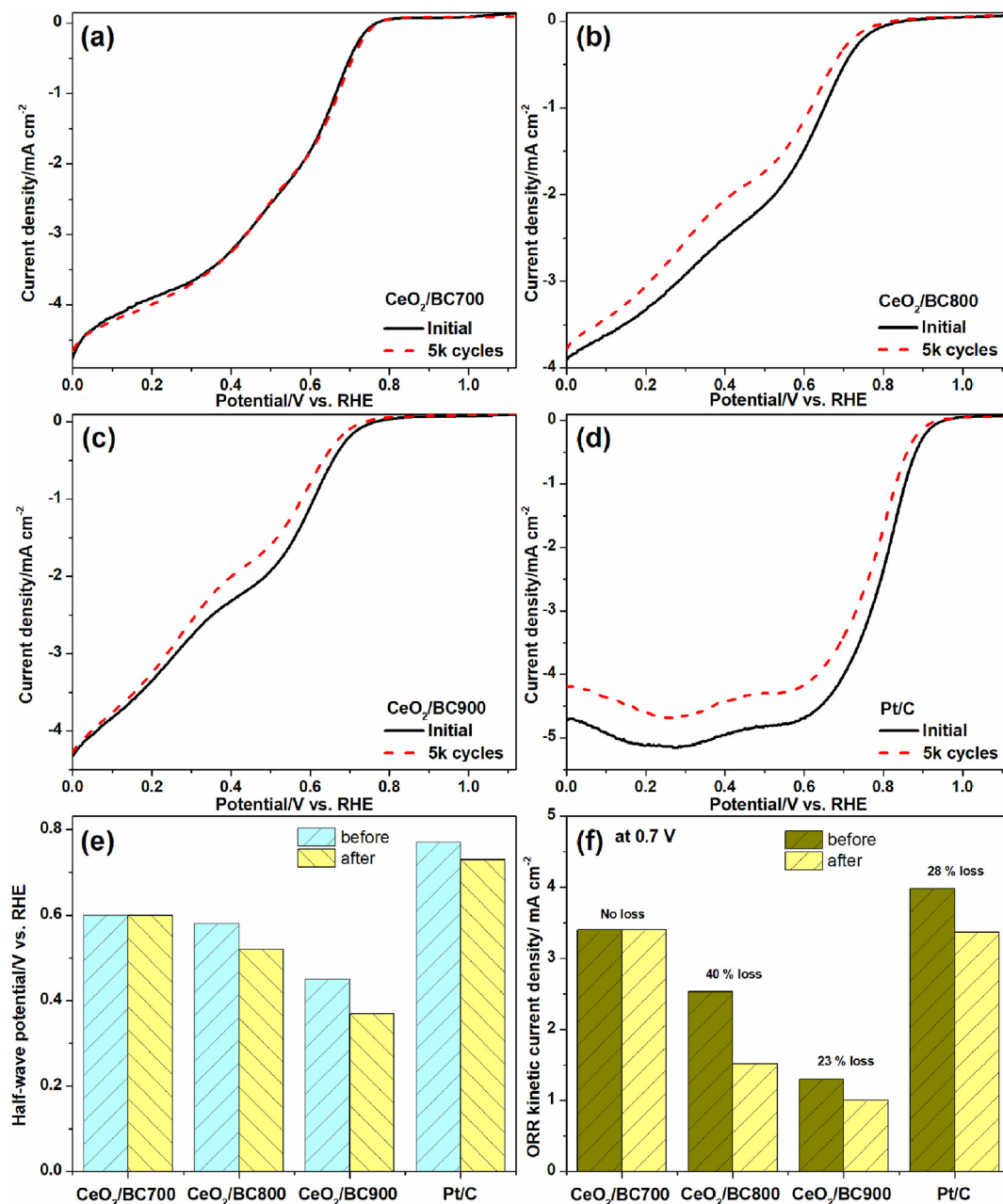
Fig. 8 − ADT-LSV profiles for (a) CeO$_2$/BC700, (b) CeO$_2$/BC800, (c) CeO$_2$/BC900 and (d) Pt/C in O$_2$ saturated 0.1 M KOH at 0.01 V s^{-1} with 1600 rpm; bar chart of (e) shift in E$_{1/2}$ and (f) ORR kinetic current density at 0.7 V vs. RHE before and after 5000 PCs.

determining step. This was well consistent with the *n* values obtained from RRDE results. This could be due to the changes in surface adsorption phenomenon over the slight structural differences at higher pyrolysis temperature of the catalysts. Particularly, the prime key indicators of E_{on}, $E_{1/2}$, and *j* (at 0.4 V) values of CeO$_2$/BC700, 800 and 900 catalysts were compared with the reported CeO$_2$ based catalysts from recent literatures and summarized in Table S1. Additionally, the j_k values are calculated to assess the electrocatalytic activity for ORR by the following Eq. (8) [67],

$$j_k = \frac{j \times j_p}{j - j_p} \qquad (8)$$

where, j_p is the current density at 0.7 V vs. RHE and *j* is the disc current density. The CeO$_2$/BC700 exhibits superior performance with the highest j_k (at 0.7 V) value of 3.4 mA cm^{-2} compared to CeO$_2$/BC800 (2.5 mA cm^{-2}), CeO$_2$/BC900 (1.3 mA cm^{-2}) and BC (1.03 mA cm^{-2}) and better than the reported catalysts such as CeO$_2$/NrGO (7.2 mA cm^{-2}) and CeO$_2$/

rGO (3.2 mA cm^{-2}) at −0.7 V vs. Ag/AgCl [15], BC-Ce-2 (0.92 mA cm^{-2}) and Pt/C (1.1 mA cm^{-2}) at $E_{1/2}$ value [47], from recent literatures. The Tafel plots given in Fig. 7f shows that the CeO$_2$/BC700 holds the Tafel slope value of 96 mV dec^{-1} found comparatively lower than Pt/C (120 mV dec^{-1}) and equal or slightly higher than CeO$_2$/BC800 (96 mV/dec), CeO$_2$/BC900 (76 mV/dec) and BC (71 mV dec^{-1}) catalysts. According to the Langmuir adsorption isotherm, the low coverage of active catalyst sites at higher overpotential region indicates that the ORR follows first electron transfer as the rate determining step [25]. Based on the ORR kinetic parameters, the CeO$_2$/BC700 exhibiting improved activity, over other catalysts might be due to the substantial features on its structural morphology and the optimal pyrolysis temperature.

The long-term stability of the catalysts was assessed through potential cycling between 0.6 and 1.1 V vs. RHE at a scan rate of 0.1 V s^{-1} under O$_2$ atmosphere. Fig. 8a–d shows the LSV curves recorded for CeO$_2$/BC (700, 800 and 900 °C) and Pt/C catalysts before and after 5000 potential cycles (PCs). After 5000 PCs, there was no significant change in ORR polarization curves for CeO$_2$/BC700, which resulted no change in key indicators of E_{on}, $E_{1/2}$ and j_k values. Whereas, the order of stability was determined as a function of negative shift of $E_{1/2}$ and the percentage of j_k loss was found as Pt/C (40 mV vs. 11%) > CeO$_2$/BC800 (50 mV vs. 15%)> CeO$_2$/BC900 (60 mV vs. 18%). In addition to this, the morphological change of CeO$_2$/BC700 catalyst over the potential cycling (after 5000 cycles) was studied by TEM images and presented in Fig. S5. From the respective TEM images, the spindle-shaped morphology of CeO$_2$ was retained with slightly wrinkled surface probably due to the continuous potential cycling, which resulted a negligible difference in ORR performance.

The bar chart of Fig. 8e and f shown the negative shift of $E_{1/2}$ and percentage of ORR kinetic current density (j_k at 0.7 V vs. RHE) loss for all the catalysts after ADT test. This result reveals that the CeO$_2$/BC700 (j_k: no loss & $E_{1/2}$: no shift) has extended stability over 5000 PCs compared to CeO$_2$/BC800 (j_k: 40% loss & $E_{1/2}$: -60 mV shift) and CeO$_2$/BC800 (j_k: 23% loss & $E_{1/2}$: -80 mV shift) catalysts, including standard Pt/C (j_k: 28% loss & $E_{1/2}$: -40 mV shift). Moreover, the stability of CeO$_2$/BC700 much better than the reported CeO$_2$ based ORR catalysts such as Co−CeO2/N-CNR (−28 mV $E_{1/2}$ shift and ~5% loss of j after 5000 PCs) [19], Ce−HPCN (−3 mV $E_{1/2}$ shift and no loss of j after 1000 PCs) [27], 20 wt % GDC-PBC (−5 mV $E_{1/2}$ shift and ~4% loss of j after 200 PCs) [68], CeO$_2$@MnO$_2$ (−29 mV $E_{1/2}$ shift and ~6% loss of j after 5000 PCs) [20], Co$_3$O$_4$−CeO$_2$/KB (−16 mV $E_{1/2}$ shift and 10% loss of j after 2000 PCs) [30] in KOH medium.

From the physicochemical characterization results and the calculated ORR kinetic parameters, the CeO$_2$/BC700 catalyst showed a superior ORR activity and stability compared to all other catalysts. This improved electrocatalytic performance might be due to the following factors, (i) the high crystallinity and stability of (111) facet and the apparent percentage of Ce^{3+} can acquire more oxygen vacancy for increased oxygen mass transport [14,50,61,69], which were clearly demonstrated from XRD, XPS and Raman spectra; (ii) the coupling effect [15] between CeO$_2$ and carbon support might be induced through the in-situ synthesis approach, evidenced by XPS results; (iii) the nature of defect-rich carbon with a high specific surface area can afford more active sites as confirmed by Raman spectra

and BET results [14,70]; (iv) the higher proportion of graphitic N and pyridinic N are the crucial factors for the improved conductivity [14,66]; (v) the facile electron transfer through delocalized π-electrons between N and carbon skeleton was observed from XPS studies [69]; (vi) the spindle-shape of CeO$_2$ with sharp edges and (111) orientation as predominant plane was noticed from SEM and TEM images; and (vii) the ECSA value clearly depicts the accessibility of more active sites among the other catalysts, which are considered as the key features for improved ORR activity and stability of CeO$_2$/BC700. In a nutshell, the structural morphology, crystalline features, surface composition with enriched oxygen vacancy, self-doped N & P and the electrochemical kinetic parameters such as onset potential, half-wave potential, kinetic current density, n value, HO$_2^-$ % with no loss after 5000 PCs are strongly proposed that the CeO$_2$/BC700 possesses an excellent capability and could be a possible candidate for ORR in KOH medium.

Conclusions

A typical choice of carbon support, *Spirulina platensis* microalgae from natural sources and simplified synthesis procedure through hydrothermal treatment was adopted to obtain spindle-shaped CeO$_2$ on carbon as ORR catalyst. CeO$_2$/BC700 exhibited improved activity with earlier E_{on} (0.79 V), $E_{1/2}$ (0.60 V) and j_k (15.08 mA cm^{-2} at 0.4 V) compared to other CeO$_2$/BC catalysts and competing with standard Pt/C. In addition, the n values are near 4-electron transfer from K-L plots and RRDE with the lowest % of HO$_2^-$, confirming the viable electrocatalytic activity of CeO$_2$/BC700 catalyst. The high specific surface area (135.88 m^2 g^{-1}), the defective structure of mesoporous carbon (I$_D$/I$_G$: 1.1), N−C boding with delocalized π-electrons and higher proportion of graphitic N (39%) and pyridinic N (22.7%), with considerable Ce^{3+} content are key factors for the improved ORR activity of CeO$_2$/BC700 catalyst. The stability result was similar to the ORR activity with the order of CeO$_2$/BC700> CeO$_2$/BC800> CeO$_2$/BC900 and surprisingly much better than standard Pt/C catalyst. In conclusion, the improved activity and stability of spindle-shaped CeO$_2$ on biochar derived carbon (700) could be employed as a promising contender for an alternate to noble metal catalyst towards ORR in alkaline fuel cells.

Declaration of Competing Interest

The authors declare that they have no known competing financial interests or personal relationships that could have appeared to influence the work reported in this paper.

Acknowledgements

Appendix A. Supplementary data

Supplementary data to this article can be found online at https://doi.org/10.1016/j.ijhydene.2020.10.115.

REFERENCES

[1] Yan Z, Xie J, Jing J, Zhang M, Wei W, Yin S. MoO2 nanocrystals down to 5 nm as Pt electrocatalyst promoter for stable oxygen reduction reaction. Int J Hydrogen Energy 2012;37(21):15948—55.

[2] Weththasinha HABMD, Yan Z, Gao L, Li Y, Pan D, Zhang M, Lv X, Wei W, Xie J. Nitrogen doped lotus stem carbon as electrocatalyst comparable to Pt/C for oxygen reduction reaction in alkaline media. Int J Hydrogen Energy 2017;42(32):20560—7.

[3] Yan Z, Gao L, Dai C, Zhang M, Lv X, Shen PK. Metal-free mesoporous carbon with higher contents of active N and S codoping by template method for superior ORR efficiency to Pt/C. Int J Hydrogen Energy 2018;43(7):3705—15.

[4] Bhuvanendran N, Ravichandran S, Jayaseelan SS, Xu Q, Khotseng L, Su H. Improved bi-functional oxygen electrocatalytic performance of Pt—Ir alloy nanoparticles embedded on MWCNT with Pt-enriched surfaces. Energy 2020;211:118695.

[5] Bhuvanendran N, Balaji S, Zhang W, Xu Q, Pasupathi S, Su H. Improved activity and stability of Ag—Rh network-like nanoalloy as support-free electrocatalyst for oxygen reduction in alkaline fuel cells. J Renew Sustain Energy 2020;12(4):044301.

[6] Bhuvanendran N, Ravichandran S, Peng K, Jayaseelan SS, Xu Q, Su HN. Highly durable carbon supported Fe-Nnanocrystals feature as efficient bi-functional oxygen electrocatalyst. Int J Energy Res 2020;44(11):8413—26.

[7] Yao D, Jao T-C, Zhang W, Xu L, Xing L, Ma Q, Xu Q, Li H, Pasupathi S, Su H. In-situ diagnosis on performance degradation of high temperature polymer electrolyte membrane fuel cell by examining its electrochemical properties under operation. Int J Hydrogen Energy 2018;43(45):21006—16.

[8] Xing L, Shi W, Su H, Xu Q, Das PK, Mao B, Scott K. Membrane electrode assemblies for PEM fuel cells: a review of functional graded design and optimization. Energy 2019;177:445—64.

[9] Ioroi T, Siroma Z, Yamazaki S-i, Yasuda K. Electrocatalysts for PEM fuel cells. Adv Energy Mater 2019;9(23):1801284.

[10] Liu D, Tao L, Yan D, Zou Y, Wang S. Recent advances on non-precious metal porous carbon-based electrocatalysts for oxygen reduction reaction. ChemElectroChem 2018;5(14):1775—85.

[11] He C, Sankarasubramanian S, Matanovic I, Atanassov P, Ramani V. Understanding the oxygen reduction reaction activity and oxidative stability of Pt supported on Nb-doped TiO2. ChemSusChem 2019;12(15):3468—80.

[12] Chen D, Chen C, Baiyee ZM, Shao Z, Ciucci F. Nonstoichiometric oxides as low-cost and highly-efficient oxygen reduction/evolution catalysts for low-temperature electrochemical devices. Chem Rev 2015;115(18):9869—921.

[13] Gao H, Liao S, Zhang Y, Wang L, Zhang L. Methanol tolerant core-shell RuFeSe@Pt/C catalyst for oxygen reduction reaction. Int J Hydrogen Energy 2017;42(32):20658—68.

[14] Yang L, Cai Z, Hao L, Xing Z, Dai Y, Xu X, Pan S, Duan Y, Zou J. Nano Ce2O2S with highly enriched oxygen-deficient Ce3+ sites supported by N and S dual-doped carbon as an active oxygen-supply catalyst for the oxygen reduction reaction. ACS Appl Mater Interfaces 2017;9(27):22518—29.

[15] Soren S, Mohaptra BD, Mishra S, Debnath AK, Aswal DK, Varadwaj KSK, Parhi P. Nano ceria supported nitrogen doped graphene as a highly stable and methanol tolerant electrocatalyst for oxygen reduction. RSC Adv 2016;6(80):77100—4.

[16] Melchionna M, Bevilacqua M, Fornasiero P. The electrifying effects of carbon-CeO2 interfaces in (electro)catalysis. Mater Today Adv 2020;6:100050.

[17] Montini T, Melchionna M, Monai M, Fornasiero P. Fundamentals and catalytic applications of CeO2-based materials. Chem Rev 2016;116(10):5987—6041.

[18] Wang J, Xiao X, Liu Y, Pan K, Pang H, Wei S. The application of CeO2-based materials in electrocatalysis. J Mater Chem 2019;7(30):17675—702.

[19] Sivanantham A, Ganesan P, Shanmugam S. A synergistic effect of Co and CeO2 in nitrogen-doped carbon nanostructure for the enhanced oxygen electrode activity and stability. Appl Catal, B 2018;237:1148—59.

[20] Yang J, Wang J, Zhu L, Gao Q, Zeng W, Wang J, Li Y. Enhanced electrocatalytic activity of a hierarchical CeO2 @MnO2 core-shell composite for oxygen reduction reaction. Ceram Int 2018;44(18):23073—9.

[21] Wang W, Dong Y, Yang Y, Chai D, Kang Y, Lei Z. CeO2 overlapped with nitrogen-doped carbon layer anchoring Pt nanoparticles as an efficient electrocatalyst towards oxygen reduction reaction. Int J Hydrogen Energy 2018;43(27):12119—28.

[22] Du C, Gao X, Cheng C, Zhuang Z, Li X, Chen W. Metal organic framework for the fabrication of mutually interacted PtCeO2C ternary nanostructure: advanced electrocatalyst for oxygen reduction reaction. Electrochim Acta 2018;266:348—56.

[23] Masuda T, Fukumitsu H, Fugane K, Togasaki H, Matsumura D, Tamura K, Nishihata Y, Yoshikawa H, Kobayashi K, Mori T, Uosaki K. Role of cerium oxide in the enhancement of activity for the oxygen reduction reaction at Pt—CeOx nanocomposite electrocatalyst - an in situ electrochemical X-ray absorption fine structure study. J Phys Chem C 2012;116(18):10098—102.

[24] Altamirano-Gutiérrez A, Fernández AM, Rodríguez Varela FJ. Preparation and characterization of Pt-CeO2 and Pt-Pd electrocatalysts for the oxygen reduction reaction in the absence and presence of methanol in alkaline medium. Int J Hydrogen Energy 2013;38(28):12657—66.

[25] Sun S, Xue Y, Wang Q, Li S, Huang H, Miao H, Liu Z. Electrocatalytic activity of silver decorated ceria microspheres for the oxygen reduction reaction and their application in aluminium—air batteries. Chem Commun 2017;53(56):7921—4.

[26] Kwon K, Lee KH, Jin S-a, You DJ, Pak C. Ceria-promoted oxygen reduction reaction in Pd-based electrocatalysts. Electrochem Commun 2011;13(10):1067—9.

[27] Xia W, Li J, Wang T, Song L, Guo H, Gong H, Jiang C, Gao B, He J. The synergistic effect of Ceria and Co in N-doped leaf-like carbon nanosheets derived from a 2D MOF and their

enhanced performance in the oxygen reduction reaction. Chem Commun 2018;54(13):1623–6.

[28] He X, Yi X, Yin F, Chen B, Li G, Yin H. Less active CeO2 regulating bifunctional oxygen electrocatalytic activity of Co3O4@N-doped carbon for Zn–air batteries. J Mater Chem 2019;7(12):6753–65.

[29] Zhang Z, Gao D, Xue D, Liu Y, Liu P, Zhang J, Qian J. Co and CeO2 co-decorated N-doping carbon nanofibers for rechargeable Zn–air batteries. Nanotechnology 2019;30(39):395401.

[30] Liu K, Huang X, Wang H, Li F, Tang Y, Li J, Shao M. Co3O4–CeO2/C as a highly active electrocatalyst for oxygen reduction reaction in Al–air batteries. ACS Appl Mater Interfaces 2016;8(50):34422–30.

[31] Yu Y, He B, Liao Y, Yu X, Mu Z, Xing Y, Xing S. Preparation of hollow CeO2/CePO4 with nitrogen and phosphorus Co-doped carbon shells for enhanced oxygen reduction reaction catalytic activity. ChemElectroChem 2018;5(5):793–8.

[32] Yu Y, Peng X, Ali U, Liu X, Xing Y, Xing S. Facile route to achieve bifunctional electrocatalysts for oxygen reduction and evolution reactions derived from CeO2 encapsulated by the zeolitic imidazolate framework-67. Inorg Chem Front 2019;6(11):3255–63.

[33] Li J-C, Maurya S, Kim YS, Li T, Wang L, Shi Q, Liu D, Feng S, Lin Y, Shao M. Stabilizing single-atom iron electrocatalysts for oxygen reduction via ceria confining and trapping. ACS Catal 2020;10(4):2452–8.

[34] Hota I, Soren S, Mohapatra BD, Debnath AK, Muthe KP, Varadwaj KSK, Parhi P. Mn-doped ceria/reduced graphene oxide nanocomposite as an efficient oxygen reduction reaction catalyst. J Electroanal Chem 2019;851:113480.

[35] Sun L, Zhou L, Yang C, Yuan Y. CeO2 nanoparticle-decorated reduced graphene oxide as an efficient bifunctional electrocatalyst for oxygen reduction and evolution reactions. Int J Hydrogen Energy 2017;42(22):15140–8.

[36] Assumpção MHMT, Moraes A, De Souza RFB, Calegaro ML, Lanza MRV, Leite ER, Cordeiro MAL, Hammer P, Santos MC. Influence of the preparation method and the support on H2O2 electrogeneration using cerium oxide nanoparticles. Electrochim Acta 2013;111:339–43.

[37] Soren S, Hota I, Debnath AK, Aswal DK, Varadwaj KSK, Parhi P. Oxygen reduction reaction activity of microwave mediated solvothermal synthesized CeO2/g-C3N4 nanocomposite. Front Chem 2019;7(403):1–10.

[38] Peng W, Zhao L, Zhang C, Yan Y, Xian Y. Controlled growth cerium oxide nanoparticles on reduced graphene oxide for oxygen catalytic reduction. Electrochim Acta 2016;191:669–76.

[39] Wang G, Peng H, Qiao X, Du L, Li X, Shu T, Liao S. Biomass-derived porous heteroatom-doped carbon spheres as a high-performance catalyst for the oxygen reduction reaction. Int J Hydrogen Energy 2016;41(32):14101–10.

[40] Peng K, Bhuvanendran N, Ravichandran S, Zhang W, Ma Q, Xing L, Xu Q, Khotseng L, Su H. Carbon supported PtPdCr ternary alloy nanoparticles with enhanced electrocatalytic activity and durability for methanol oxidation reaction. Int J Hydrogen Energy 2020;45(43):22752–60.

[41] Kandasamy S, Zhang B, He Z, Chen H, Feng H, Wang Q, Wang B, Ashokkumar V, Siva S, Bhuvanendran N, Krishnamoorthi M. Effect of low-temperature catalytic hydrothermal liquefaction of Spirulina platensis. Energy 2020;190:116236.

[42] Ravichandran S, Bhuvanendran N, Zhang W, Xu Q, Khotseng L, Su H. Comprehensive studies on the effect of reducing agents on electrocatalytic activity and durability of platinum supported on carbon support for oxygen reduction reaction. J Electrochem En Conv Stor 2020;17(3).

[43] Ma R, Jahurul Islam M, Amaranatha Reddy D, Kim TK. Transformation of CeO2 into a mixed phase CeO2/Ce2O3 nanohybrid by liquid phase pulsed laser ablation for enhanced photocatalytic activity through Z-scheme pattern. Ceram Int 2016;42(16):18495–502.

[44] Zhang D-E, Zhang X-J, Ni X-M, Song J-M, Zheng H-G. Optical and electrochemical properties of CeO2 spindles. ChemPhysChem 2006;7(12):2468–70.

[45] Niu X. Hydrothermal synthesis and optical properties of the monodisperse spindle-shaped CeO2 microstructures. Russ J Phys Chem 2018;92(4):768–71.

[46] Hailstone RK, DiFrancesco AG, Leong JG, Allston TD, Reed KJ. A study of lattice expansion in CeO2 nanoparticles by transmission electron microscopy. J Phys Chem C 2009;113(34):15155–9.

[47] Pi L, Jiang R, Cai W, Wang L, Wang Y, Cai J, Mao X. Bionic preparation of CeO2-encapsulated nitrogen self-doped biochars for highly efficient oxygen reduction. ACS Appl Mater Interfaces 2020;12(3):3642–53.

[48] Bhuvanendran N, Ravichandran S, Zhang W, Ma Q, Xu Q, Khotseng L, Su H. Highly efficient methanol oxidation on durable PtxIr/MWCNT catalysts for direct methanol fuel cell applications. Int J Hydrogen Energy 2020;45(11):6447–60.

[49] Xie Y, Wu J, Jing G, Zhang H, Zeng S, Tian X, Zou X, Wen J, Su H, Zhong C-J, Cui P. Structural origin of high catalytic activity for preferential CO oxidation over CuO/CeO2 nanocatalysts with different shapes. Appl Catal, B 2018;239:665–76.

[50] Dehkhoda AM, Ellis N, Gyenge E. Electrosorption on activated biochar: effect of thermo-chemical activation treatment on the electric double layer capacitance. J Appl Electrochem 2014;44(1):141–57.

[51] Ravichandran S, Bhuvanendran N, Zhang W, Xu Q, Khotseng L, Su H. Comprehensive studies on the effect of reducing agents on electrocatalytic activity and durability of platinum supported on carbon support for oxygen reduction reaction. J Electrochem En Conv Stor 2020;17(3):031012.

[52] Xie Q, Zhang H, Kang J, Cheng J, Zhang Q, Wang Y. Oxidative dehydrogenation of propane to propylene in the presence of HCl catalyzed by CeO2 and NiO-modified CeO2 nanocrystals. ACS Catal 2018;8(6):4902–16.

[53] Huang W, Gao Y. Morphology-dependent surface chemistry and catalysis of CeO2 nanocrystals. Catal. Sci. Technol 2014;4(11):3772–84.

[54] Capdevila-Cortada M, Vilé G, Teschner D, Pérez-Ramírez J, López N. Reactivity descriptors for ceria in catalysis. Appl Catal, B 2016;197:299–312.

[55] Hasan Z, Cho D-W, Chon C-M, Yoon K, Song H. Reduction of p-nitrophenol by magnetic Co-carbon composites derived from metal organic frameworks. Chem Eng J 2016;298:183–90.

[56] Li B, Gu T, Ming T, Wang J, Wang P, Wang J, Yu JC. (Gold core) @(ceria shell) nanostructures for plasmon-enhanced catalytic reactions under visible light. ACS Nano 2014;8(8):8152–62.

[57] Peng K, Bhuvanendran N, Ravichandran S, Xu Z, Zhang W, Ma Q, Xu Q, Khotseng L, Su H. Sewage sludge-derived Fe- and N-containing porous carbon as efficient support for Pt catalyst with superior activity towards methanol electrooxidation. Int J Hydrogen Energy 2020;45(16):9795–802.

[58] Wang Q, Zhang X, Lv R, Chen X, Xue B, Liang P, Huang X. Binder-free nitrogen-doped graphene catalyst air-cathodes for microbial fuel cells. J Mater Chem 2016;4(32):12387–91.

[59] Wang W, Li J, Kang Y, Wang F, Song J, Lei Z. Facile and scalable preparation of nitrogen, phosphorus codoped nanoporous carbon as oxygen reduction reaction electrocatalyst. Electrochim Acta 2017;248:11–9.

[60] Hu Z, Liu X, Meng D, Guo Y, Guo Y, Lu G. Effect of ceria crystal plane on the physicochemical and catalytic properties of Pd/ceria for CO and propane oxidation. ACS Catal 2016;6(4):2265—79.

[61] Aliotta C, Liotta LF, La Parola V, Martorana A, Muccillo ENS, Muccillo R, Deganello F. Ceria-based electrolytes prepared by solution combustion synthesis: the role of fuel on the materials properties. Appl Catal, B 2016;197:14—22.

[62] Xu Q, Zhang F, Xu L, Leung P, Yang C, Li H. The applications and prospect of fuel cells in medical field: a review. Renew Sustain Energy Rev 2017;67:574—80.

[63] Ullah N, Shah SA, Xie M, Rasheed HU, Oluigbo CJ, Jiang D, Xu YG, Xie JM. 3D graphene decorated with hexagonal micro-coin of Co(OH)(2): a competent electrocatalyst for hydrogen and oxygen evolution reaction. Int J Hydrogen Energy 2019;44(29):14770—9.

[64] Jayaseelan SS, Bhuvanendran N, Xu Q, Su H. Co3O4 nanoparticles decorated Polypyrrole/carbon nanocomposite as efficient bi-functional electrocatalyst for electrochemical water splitting. Int J Hydrogen Energy 2020;45(7):4587—95.

[65] Narayanamoorthy B, Linkov V, Sita C, Pasupathi S. Pt3M (M: Co, Ni and Fe) bimetallic alloy nanoclusters as support-free electrocatalysts with improved activity and durability for dioxygen reduction in PEM fuel cells. Electrocatalysis 2016;7(5):400—10.

[66] Xu L, Ding H, Yang X, Yan J, Li S, Li M, Fan H, Xia J. Gallic acid-assisted synthesis of nitrogen-doped carbon microspheres as efficient bifunctional materials for oxygen reduction and volumetric lithium storage. Mater Chem Front 2020;4(3):881—90.

[67] Narayanamoorthy B, Balaji S, Sita C, Pasupathi S, Eswaramoorthy M, Moon I-S. Enhanced intrinsic activity and stability of Au—Rh bimetallic nanostructures as a supportless cathode electrocatalyst for oxygen reduction in alkaline fuel cells. ACS Sustainable Chem Eng 2016;4(12):6480—90.

[68] Gui L, Wang Z, Zhang K, He B, Liu Y, Zhou W, Xu J, Wang Q, Zhao L. Oxygen vacancies-rich Ce0.9Gd0.1O2-δ decorated Pr0.5Ba0.5CoO3-δ bifunctional catalyst for efficient and long-lasting rechargeable Zn-air batteries. Appl Catal, B 2020;266:118656.

[69] Xu Z, Zhuang X, Yang C, Cao J, Yao Z, Tang Y, Jiang J, Wu D, Feng X. Nitrogen-doped porous carbon superstructures derived from hierarchical assembly of polyimide nanosheets. Adv Mater 2016;28(10):1981—7.

[70] Wu Z, Liu R, Wang J, Zhu J, Xiao W, Xuan C, Lei W, Wang D. Nitrogen and sulfur co-doping of 3D hollow-structured carbon spheres as an efficient and stable metal free catalyst for the oxygen reduction reaction. Nanoscale 2016;8(45):19086—92.